International Journal of Concrete Structures and Materials

RESEARCH Open Access

Experimental Evaluation of Shape Memory Alloy Retrofitting Effect for Circular Concrete Column Using Ultrasonic Pulse Velocity

Taemin Lee[1], Saebyeok Jeong[2], Ukyong Woo[1], Hajin Choi[1*] and Donghyuk Jung[3]

Abstract

The seismic performance of a concrete column retrofitted with an iron-based shape memory alloy (Fe-SMA) was evaluated under cyclic loading. In addition to structural behavior, internal damage was monitored using an ultrasonic pulse velocity test. The round shapes of three reinforced concrete (RC) columns were tested: a non-retrofitted RC column as a control, a carbon fiber-reinforced polymer (CFRP) column, and an Fe-SMA retrofitted column. During the cyclic loading test, the degradation of the column was defined based on the decrease in compressional wave velocities. The experimental results demonstrated a maximum improvement of 175% in seismic performance of the Fe-SMA retrofitted RC column compared with the controlled column. This is primarily owing to the active constraints of the SMA, which were quantified based on ultrasonic velocities. Furthermore, the surface degradation process was identified using external cracks, which were not visible in the CFRP retrofitted RC column.

Keywords: Shape memory alloy, Ultrasonic, Retrofit, Concrete column, Piloti

1 Introduction

Over the past few decades, critical seismic damage to buildings and infrastructure has been extensively reported worldwide. The brittle failure of reinforced concrete (RC) columns in low-rise piloti buildings is one type of such damage, as observed in the 2017 Pohang earthquake in Korea (AIK 2018). Generally, seismically deficient RC columns can fail in shear, flexure, or flexure–shear modes, exhibiting a limited deformation capability. A crucial and common cause for such brittle failure of RC columns is poor seismic detailing and lack of concrete confinement associated with insufficient and/or unsecured transverse reinforcement (Kim et al., 2020). Several retrofitting methods have been investigated and implemented to increase the deformation capability (i.e., ductility) of existing vulnerable RC columns. Steel jackets and fiber-reinforced polymer (FRP) sheets (Shehata et al., 2002, Seible et al., 1997, Akguzel et al., 2012, Yahiaoui et al., 2022, Vahidpour et al., 2022, Zhao et al., 2020) are the most used conventional methods that rely on passive confinement mechanisms, in which confinement is triggered by the lateral expansion of concrete. Concrete in a confined region is subjected to triaxial compression and can exhibit significantly enhanced compressive behavior. However, because of its intrinsic mechanism, which requires concrete dilation, passive confinement inevitably involves concrete damage; therefore, passively confined RC columns may have limited retrofitting effects with a certain level of seismic damage (Xiao et al. 2003; Saadatmanesh et al., 1994; Ma et al., 2017; Sarno et al., 2006). Furthermore, the application of these conventional materials requires additional demanding operations, such as the welding of steel jackets or the use of wet process materials (mortar or epoxy resin), which are labor-intensive and time-consuming for field applications.

Journal information: ISSN 1976-0485 / eISSN 2234-1315

*Correspondence: hjchoi@ssu.ac.kr

[1] School of Architecture, Soongsil University, Seoul, Republic of Korea
Full list of author information is available at the end of the article

Recent studies have demonstrated the significant potential of shape memory alloys (SMAs) as smart retrofitting materials for RC columns. Shin and Andrawes, (2010) studied the use of nickel–titanium (NiTi)-based SMA wires for the seismic retrofitting of RC columns. In that study, NiTi-SMA wires were used to apply heat-activated prestressing to the plastic hinge region of the RC columns. This active confinement technique provides a confining pressure to concrete in advance without requiring concrete dilation; thus, it is useful for delaying concrete damage and enhancing the deformation capacity of RC columns. The efficacy of SMA-based active confinement has been experimentally verified through quasi-static and dynamic tests of RC columns (Choi et al., 2012; Jung et al., 2018; Shin & Andrawes, 2011). In these tests, SMA confinement prevented the spalling and crushing of concrete and significantly improved the ductility of the columns. The superior effect of SMA confinement compared with passive confinement provided by FRP has been clearly demonstrated in experimental studies (Shin & Andrawes, 2010, 2011). Another promising aspect of SMA confinement is its ease and rapidity because the confinement can be instantly activated through simple heating of the pre-strained SMA. Fig. 1 depicts the mechanisms of active and passive confinement methods and how active confinement can suppress the lateral expansion and damage of concrete.

However, from a practical and economical perspective, the use of NiTi-SMA in the construction field is not feasible because of its excessively high manufacturing and processing costs. In recent years, low-price iron-based SMAs (Fe-SMAs) have emerged and gained significant interest as attractive substitutes for NiTi-SMAs. With a price of only 5%–10% that of NiTi-SMAs, Fe-SMAs are available for mass production and have a satisfactory prestressing capability (Cladera et al., 2014). Currently, various research and development activities are being undertaken on the application of Fe-SMAs to civil infrastructure systems. Cladera et al., (2014) studied the development and thermomechanical properties of Fe–Mn–Si alloys suitable for civil engineering. Czaderski et al., (2014) experimentally evaluated the pre-stressing effect of Fe–Mn–Si alloys, and this technique was further studied for the flexural strengthening of RC beams by several researchers (Hong et al., 2018a, 2018b; Rojob & El-Hacha, 2017; Shahverdi et al., 2016). Zerbe et al., (2017) and Ji et al., (2020) used an Fe–Mn–Si SMA for the external or internal confinement of RC columns. The tests indicated that the Fe-SMA was effective in increasing the strength and ultimate deformation of RC columns under axial compression. However, previous studies focused only on the retrofitting effect of Fe-SMAs for axial compression; thus, further research on the flexural and shear retrofitting of Fe-SMAs for RC columns is required.

In this study, RC columns retrofitted with carbon FRP (CFRP) sheets and Fe-SMA strips were tested under quasi-static cyclic loading. During the test, the retrofitting effect was evaluated using the dry-coupled ultrasonic pulse velocity (UPV) test. At a pre-defined target drift ratio of the columns, internal damage was monitored by converting the ultrasonic velocity into the dynamic modulus of the materials. The uniqueness of this study was (1) to monitor the degradation progress of RC columns using dry-coupled UPV test and (2) to demonstrate the retrofitting effect with respect to the internal damage of the columns assessed using non-destructive evaluation. The experimental results proved that the proposed Fe-SMA retrofitting method has both structural and practical benefits. In addition, the results from the non-destructive inspection will broaden our understanding of the structural behaviors and damage propagation of columns under cyclic loading.

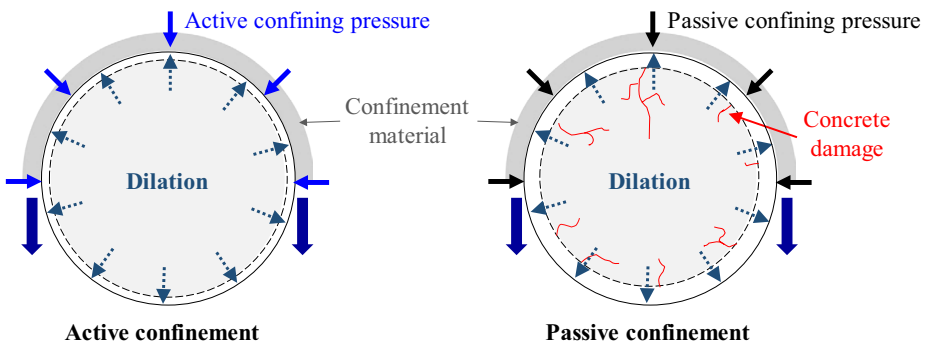

Fig. 1 Comparison of active and passive confinement methods

2 Methodology

2.1 Active Confinement Using Shape Memory Alloys

An SMA is a smart material that has exceptional thermomechanical characteristics known as the shape memory effect (SME). Many researchers have employed the SME for pre-stressing techniques for concrete structures (Choi et al., 2012; Hong et al., 2018a; Janke et al., 2005; Jung et al., 2018; Rojob & El-Hacha, 2017; Shahverdi et al., 2016; Shin & Andrawes, 2011). The SME is activated when the crystal structure of the SMA transforms from martensite to austenite when heated. At temperatures below the martensite finish temperature (M_f), the SMA is in the martensite phase and can be permanently deformed after being loaded and unloaded beyond the elastic range. At temperatures above the austenite start temperature (A_s), the pre-strained SMA recovers its original shape as the austenite phase begins to form, and shape recovery is completed at the austenite finish temperature (A_f). When shape recovery is physically restrained, a large recovery stress (i.e., pre-stress) is generated in the SMA. Fig. 2 depicts how the recovery stress is induced from the pre-strained SMA. For SMA-based active confinement, pre-strained SMAs can be wrapped around an RC column and firmly anchored. When heated, the SMAs restrained by the column provide a lateral confining pressure to the column. Fig. 3 shows the SMA confinement used to retrofit the plastic hinge regions of the circular RC columns in which crushing of concrete is expected to occur due to excessive flexural deformation.

2.2 Ultrasonic Pulse Velocity Test

The UPV test is a standard method in which the compressional wave (or pressure, longitudinal wave) velocity is measured through concrete elements (ASTM C597, 2016); this velocity is typically in the range of 3700–4200 m/s for ordinary concrete (Naik et al., 2004). The compressional wave velocity (V_c) is related to the mechanical properties of the materials, and the relationship is expressed as

$$V_c = \sqrt{\frac{E(1-\nu)}{\rho(1+\nu)(1-2\nu)}}, \tag{1}$$

where E, ρ, and ν are the elastic modulus, density, and Poisson's ratio of a material, respectively. With minimal variation in the density and Poisson's ratio of materials, the wave velocity frequently correlates with the elastic modulus of the material. Therefore, the increment and reduction in the velocity imply the healing and degradation of materials with respect to the elastic modulus.

Ultrasonic tests in concrete are frequently limited by the applied frequency band and coupling procedure. Concrete is a typical composite material consisting of cement, several mineral admixtures, and aggregates such as sand and gravel. In particular, coarse aggregates cause strong scattering, and high-frequency ultrasonic waves do not propagate through concrete. Therefore, compared with the maximum size of coarse aggregates, a larger wavelength of ultrasound with a frequency of less than 100 kHz has been applied to concrete inspection (Chekroun et al., 2009; Ohdaira & Masuzawa, 2000; Saffar & Abdullah, 2013). Conventional ultrasonic transducers are fabricated from piezoelectric materials (e.g., lead zirconate titanate, PZT). The transducers at low frequencies have a large diameter because piezoelectric materials gradually resonate based on their shape or boundary. The coupling procedure for large transducers is complex, where a gel-type coupling material is required to reduce the acoustic impedance mismatch between the

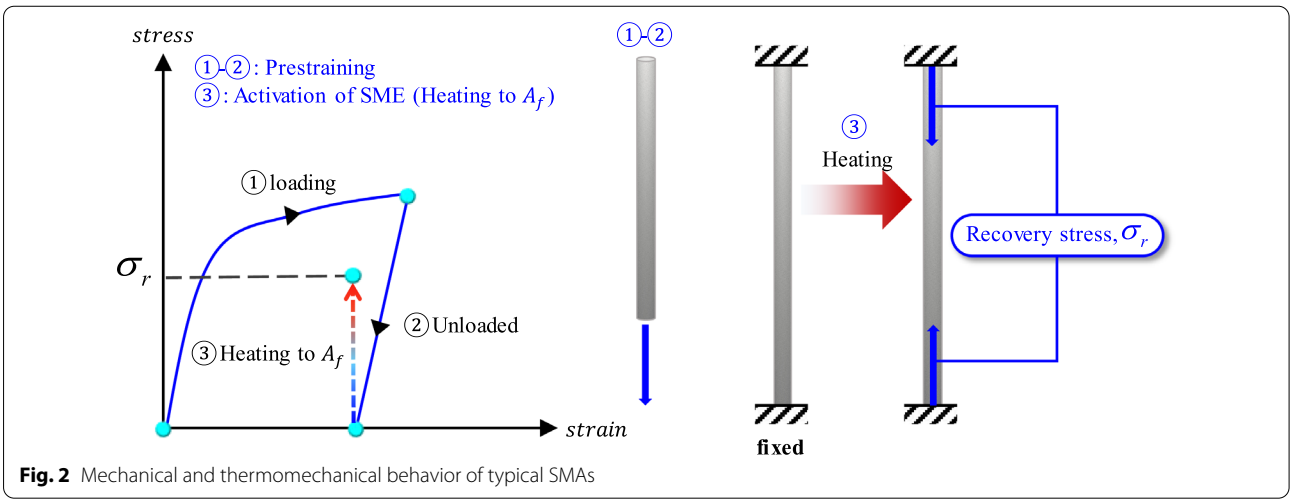

Fig. 2 Mechanical and thermomechanical behavior of typical SMAs

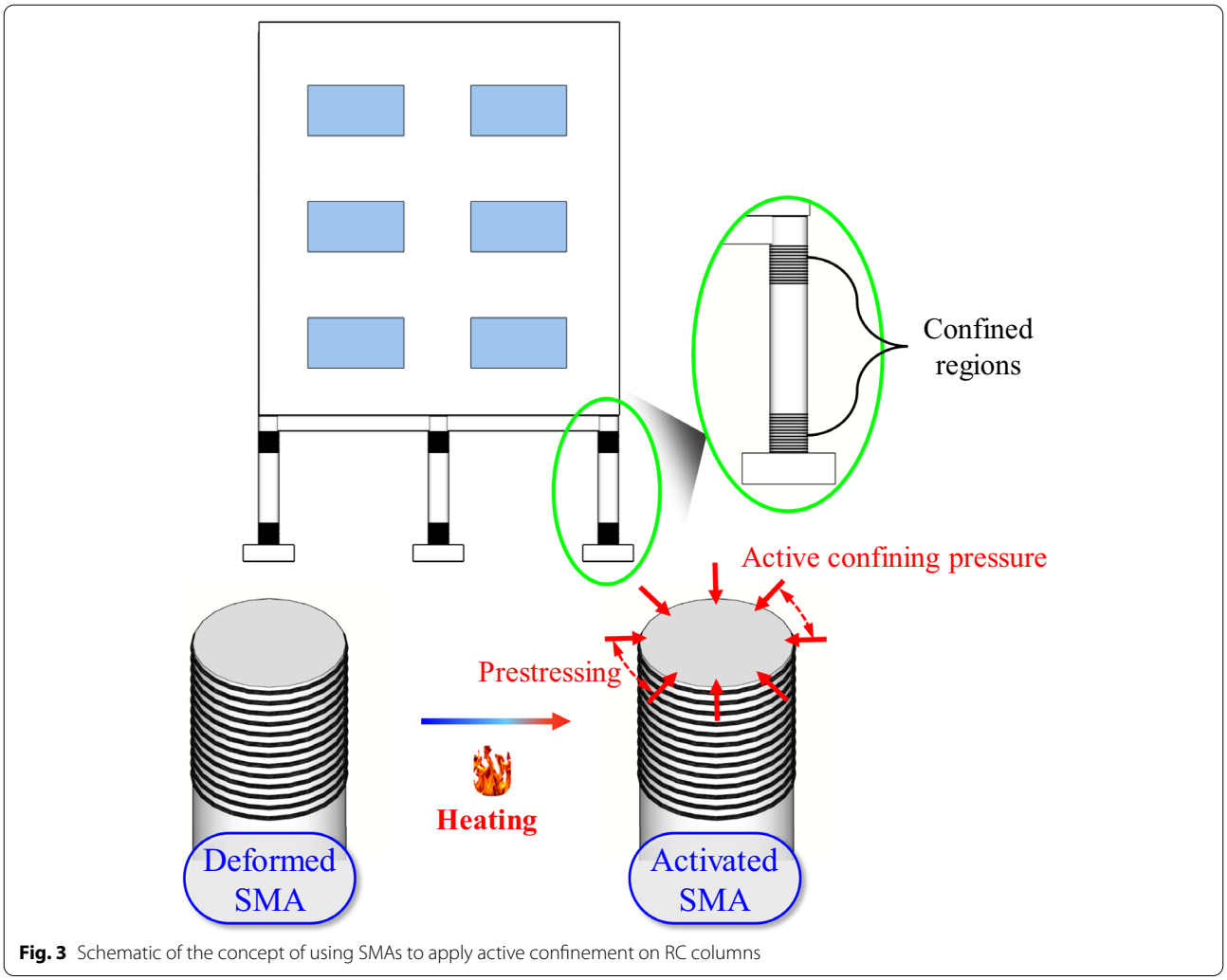

Fig. 3 Schematic of the concept of using SMAs to apply active confinement on RC columns

transducer and concrete. The acoustic impedance (Z) is the intrinsic material property, expressed as

$$Z = \rho V_c. \tag{2}$$

The reflection coefficient, which indicates the acoustic energy reflection rate, can be calculated using the acoustic impedances of materials (Z_1 and Z_2) as

$$R = \frac{Z_2 - Z_1}{Z_2 + Z_1}. \tag{3}$$

Table 1 lists the acoustic impedances of PZT, air, and concrete. Note that the air gap represents the insufficient coupling between the ultrasonic transducer and concrete. Absolute values of the reflection coefficients close to 1 indicate that most of the wave energy is reflected.

Table 1 Acoustic properties of PZT, air, and concrete

Material	Acoustic impedance (MRayl)	Reflection coefficient calculated using Eq. (3)		
		PZT to air	Air to concrete	PZT to concrete
PZT-4	36.15	− 0.999	–	− 0.52 to − 0.62
Air at 25 °C	0.00042		0.999	
Concrete	8.36–11.3	–		

*A negative reflection coefficient represents the phase inversion of the wave

Therefore, coupling materials are required to reduce the energy transmission when using the UPV.

Fig. 4 Applied dry-coupled UPV transducer (ACSA A1410 Pulsar)

In this study, recently developed dry-coupled transducers were used, which significantly improved the coupling with the UPV. As shown in Fig. 4, the ultrasonic equipment consisted of seven transducers, and the tip of every transducer simultaneously generated compressional waves into the concrete. In the receiving part, the compressional waves were measured using the seven transducers, and one waveform was stored as an average of the seven. The dry-coupled transducers were handheld equipment, and the operator simply contacted the transducers to the surface of the concrete. Details of the equipment used are listed in Table 2.

3 Experiment and Results

3.1 RC Column Specimens and Seismic Retrofitting

In this study, three circular RC columns were tested under quasi-static cyclic loading. Each specimen was designed as a cantilever column with a diameter (d) of 300 mm and clear height of 1500 mm, with the assumption that the specimen represented half of an RC column

Table 2 Specification of the applied UPV equipment

Parameter	Specification
Type of ultrasonic transducers	Undamped dry-point-contact transducers
Transducer configuration	Array of seven dry-point-contact transducers
Operating frequency	50 kHz
Maximum thickness of the inspection object	2.5 m
Indication resolution of the propagation time of ultrasonic waves	0.1 μs
Indication resolution of the propagation velocity of ultrasonic waves	10 m/s

Table 3 Test specimen details

Property	Value
Section diameter (mm)	300
Effective height (mm)	1500
Axial force (kN)	254.47
Compressive strength, $f_c^{'}$ (MPa)	35.6
Yield strength of longitudinal reinforcement (MPa)	458.5
Yield strength of tie reinforcement (MPa)	431.4
Longitudinal reinforcement ratio (%)	3.2
Volumetric ratio of tie reinforcement (%)	0.05

in a piloti building. The columns were reinforced with eight D19 (19.05 mm diameter) longitudinal reinforcing bars. D10 (9.53 mm diameter) hoops were widely spaced at 300 mm along the height of the column to reflect insufficient transverse reinforcement. The 300 mm hoop space was determined based on the hoop space of the actual RC columns which showed poor seismic performance in the 2017 Pohang earthquake (Architectural Institute of Korea, 2018). The measured yield strengths of the longitudinal and transverse reinforcements were 450 and 420 MPa, respectively. The compressive strength of the concrete measured on the testing day was 36 MPa. Details of the specimens are presented in Table 3 and Fig. 5.

While one specimen (Control) remained in the as-built condition, the other two were retrofitted in the plastic hinge region. For the specimen denoted as CFRP, a CFRP sheet was selected as the retrofitting material. The CFRP sheet had a thickness (t_f) of 0.11 mm, elastic modulus (E_f) of 252,117 MPa, ultimate tensile strength (f_{fu}) of 4,513 MPa, and ultimate tensile strain (ε_{fu}) of 0.0179. Two layers of CFRP sheets were provided to apply a target passive confinement pressure ($f_{l,p}$) of 1.5 MPa, determined using Eq. (4):

$$f_{l,p} = \frac{2nt_f E_f \varepsilon_{fe}}{d}, \tag{4}$$

where n is the number of CFRP layers, and ε_{fe} is the effective hoop rupture strain of the CFRP, herein 0.004 according to ACI 440.2R-17 (2017). The height of the retrofitted region was determined to be 1.5 times the column diameter (i.e., 450 mm = 1.5 × 300 mm) according to the Caltrans guidelines (2013). During CFRP retrofitting, the concrete surface was first coated with primer, and epoxy resin was applied for the adhesion of the CFRP sheets.

For SMA confinement, Fe–17Mn–5Si–5Cr–4Ni–0.1C alloy developed by Hong et al. (2020) was used. The selected Fe-SMA was manufactured and processed into

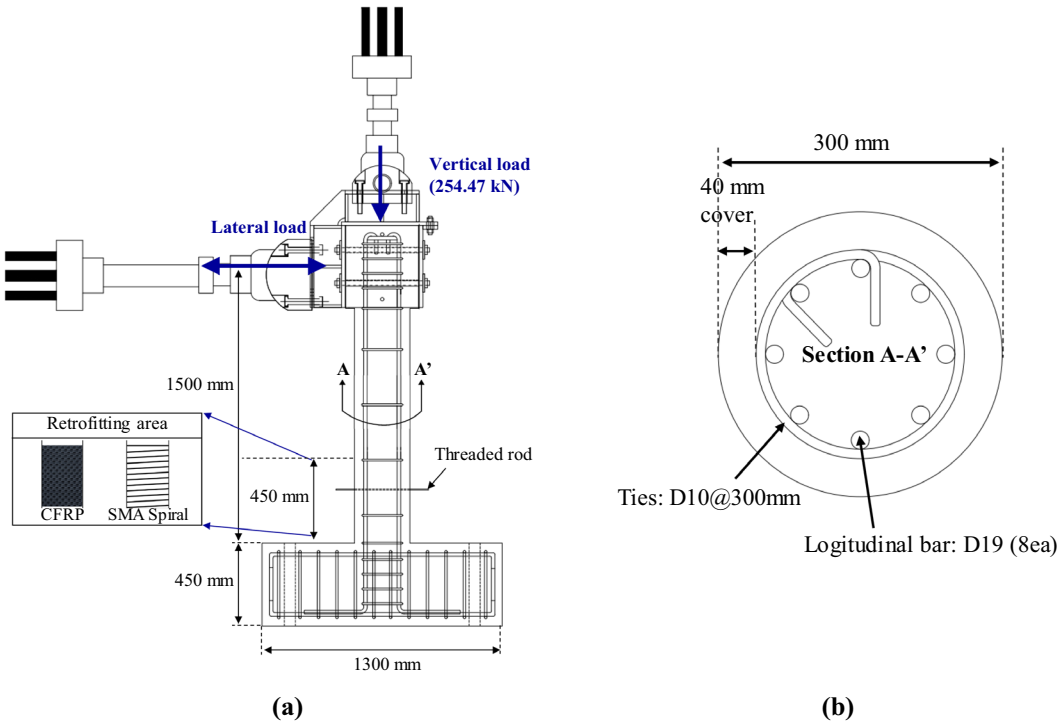

Fig. 5 Design of the RC columns and test setup. **a** Test setup; **b** cross-section of RC columns; **c** real photo of test setup

strips with a thickness of 1.95 mm and width of 5.5 mm. The Fe-SMA strips pre-strained by 4% were wrapped around the plastic hinge region of the column in a spiral form. Considering the outstanding performance of active confinement (Shin & Andrawes, 2010, 2011), compared with passive confinement, we selected a target active confinement pressure ($f_{l,a}$) of 0.75 MPa, which was half of the pressure provided to the CFRP. Based on the recovery stress (σ_r) of the selected Fe-SMA (350 MPa) measured after being heated to 250 °C, a center-to-center

spacing (s_{SMA}) of 32 mm was selected to provide an $f_{l,a}$ of 0.75 MPa, calculated using Eqs. (5) and (6) as suggested by Shin and Andrawes, (2011):

$$f_{l,a} = k_e \frac{2A_{SMA}\sigma_r}{ds_{SMA}}, \tag{5}$$

$$k_e = \frac{1 - \frac{s^*_{SMA}}{2d}}{1 - \rho_{cc}}, \tag{6}$$

where A_{SMA} and s^*_{SMA} are the cross-sectional area and clear spacing of the Fe-SMA strips, respectively, k_e is a reduction factor that accounts for unconfined regions of concrete, and ρ_{cc} is the ratio of the area of longitudinal reinforcement to the area of the gross cross-section of the column. The SME of the Fe-SMA spirals was activated by directly heating them with a butane gas torch up to 250 ℃. Fig. 6 shows images of the three test specimens after seismic retrofitting. Note that for Fe-SMA, the surface of the concrete was partially visible after the retrofitting was complete, which is beneficial for assessing visual damage after a seismic event.

Fig. 5 also shows a schematic illustration of the test setup, which used two hydraulic servo-controlled actuators. The vertical actuator applied an axial load of approximately 255 kN, corresponding to 15% of the column's axial load capacity. The horizontal actuator applied displacement-controlled lateral loads which correspond to pre-defined target drift ratios of the column. The target drift ratio incrementally increased from 0.5% to 7%, and was repeated three times at each target value in both the positive and negative directions. The loading protocol in the lateral direction determined based on ACI 374.1–05 (2014) is depicted in Fig. 7. During the testing, the columns were assumed to reach their ultimate state when the lateral load decreased below 80% of its maximum value; accordingly, the testing continued beyond the pre-defined ultimate state.

3.2 Testing Setup and Data Acquisition

In this study, the compressional wave velocity was measured from the columns before, during, and after cyclic loading. The measurements were performed at a selected zero lateral displacement, as shown in Fig. 7. For the controlled column, the initial stages of the loading cycles were thoroughly measured because the brittle failure of concrete was expected. Ultrasonic tests were performed at three locations (50, 150, and 200 mm) above the column base using dry-coupled transducers, as shown in Fig. 8. The locations were marked on the surface of the column and measured during the subsequent loading cycles. Ultrasonic transducers were placed on the surface of the CFRP column. The individual measurements took approximately 10 s and were repeated three times. The transducers were fully detached and reattached for each repetition. The waveform was wirelessly stored on a tablet computer through Bluetooth, and the averaged through-thickness velocity was calculated based on the pre-installed geometric information.

Fig. 9 shows examples of waveforms obtained from the controlled column after the drift ratios of 0%, 0.75%, and 1.5%. The arrival of waves was clearly delayed as the loading cycles increased, which was caused by internal damage to the concrete. Note that no surface cracks were identified during the loading cycles. With a column diameter of 300 mm and the arrival of waves, the

(a) (b) (c)

Fig. 6 Photos of column specimens after seismic retrofitting. **a** Control; **b** CFRP; **c** Fe-SMA

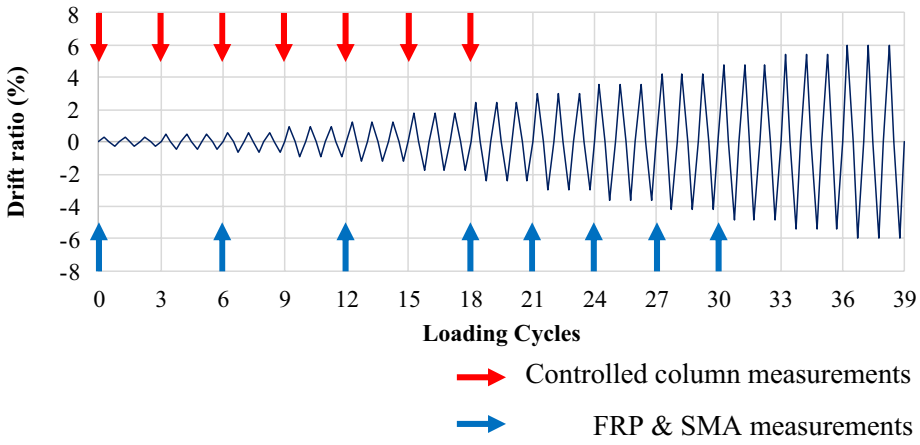

Fig. 7 Loading protocols with UPV measurement plan

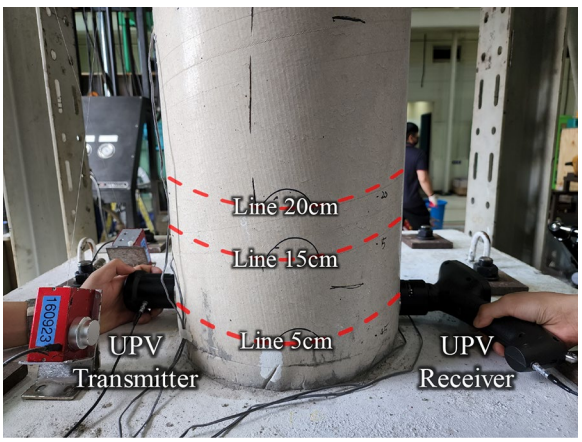

Fig. 8 Example of UPV measurements and locations

through-thickness velocity was obtained. Velocities from individual measurements are presented in the Appendix. The initial velocities of the Control, CFRP, and Fe-SMA columns at the zero-loading cycle were 4164, 4271, and 4180 m/s, respectively. The velocities were in the range of those of typical ordinary concrete (Naik et al., 2004). The degradation process of the concrete was monitored based on velocity measurements, which were normalized using the initial velocity of each specimen.

3.3 Results

3.3.1 Structural Responses of Columns

Fig. 10 shows the global lateral force–drift ratio relationships of the columns obtained from cyclic loading. Generally, the responses of the columns were similar at the

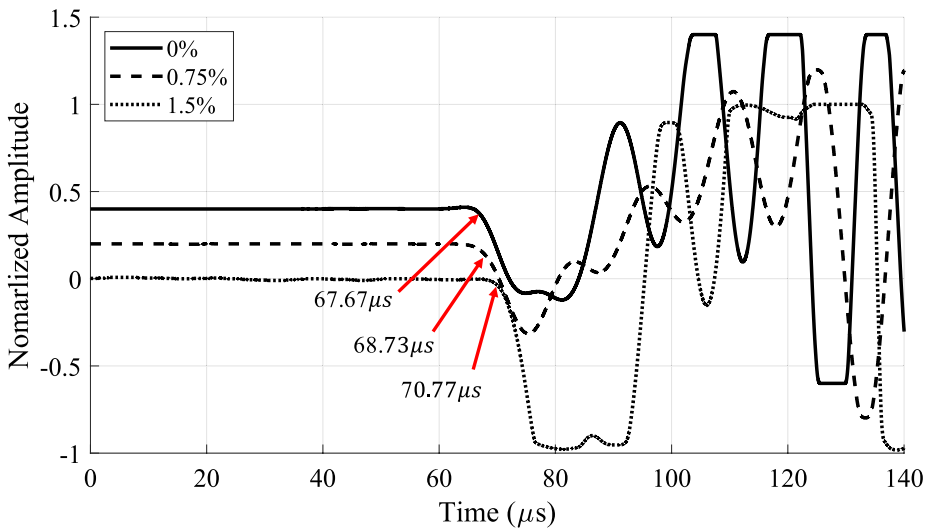

Fig. 9 Waveforms obtained at different drift ratios from the control

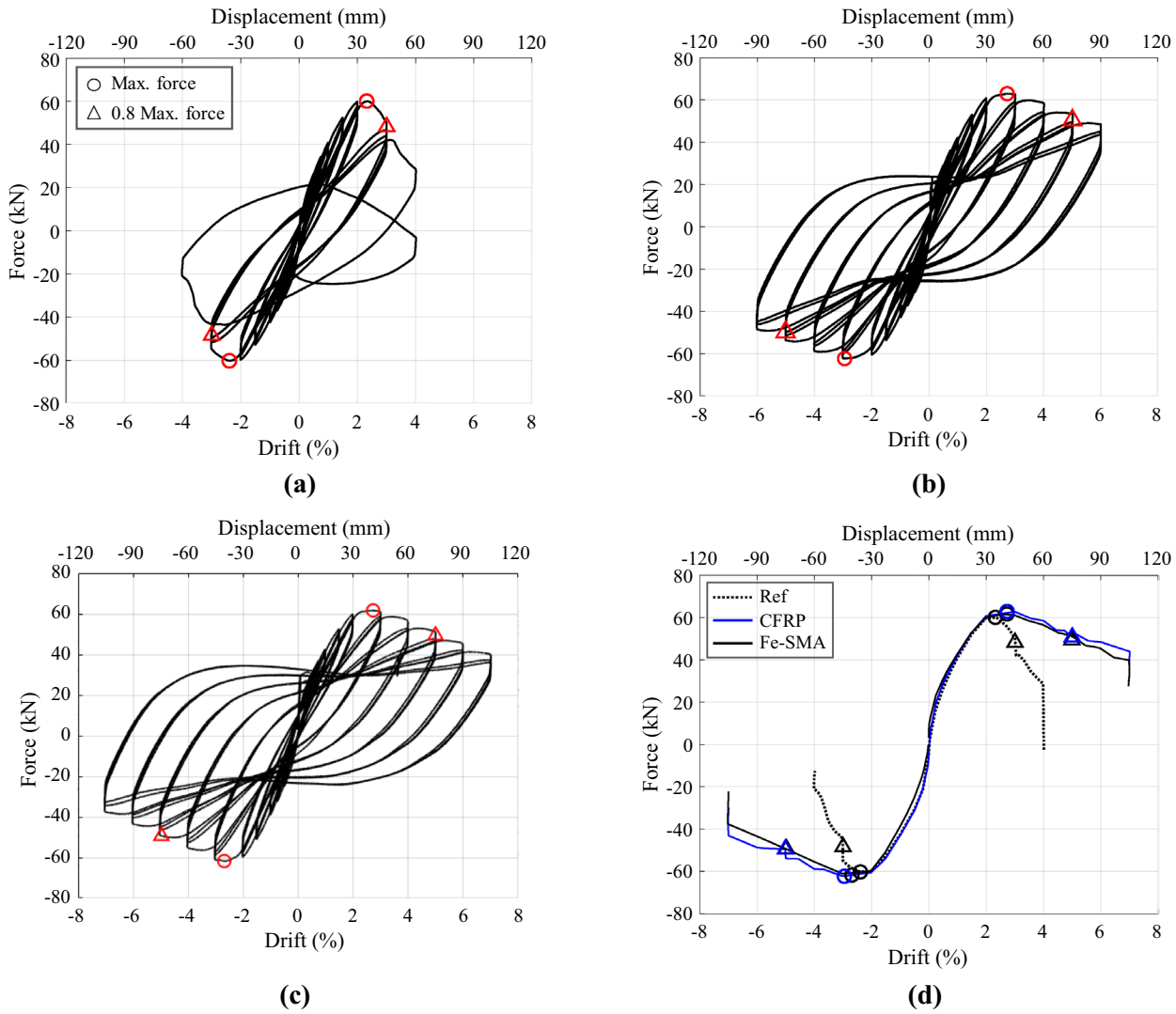

Fig. 10 Lateral force–displacement relationships of the tested columns, where the circle and triangle markers represent the maximum force and 80% of the maximum force, respectively. **a** Control; **b** CFRP; **c** Fe-SMA; **d** envelop curves

early loading stage but changed significantly after attaining the maximum forces. First, the as-built column (Control) initially exhibited stable responses with a maximum force of 60.2 kN at a drift ratio of 2.36% on average. However, after the peak, Control experienced a rapid decrease in the lateral load, recording the ultimate point at a 3% drift ratio, and it completely lost its load-carrying capacity. In contrast, the retrofitted columns exhibited stable and ductile responses. CFRP recorded an average maximum force of 62.6 kN at a drift ratio of 2.84%, exhibiting a slight strength increase of 4% compared with Control. As the drift ratio increased further, the lateral force of CFRP began to decrease, but at a much gradual rate. CFRP attained its ultimate point (50 kN) at a drift ratio of 5% on average and continued to exhibit stable responses even after the ultimate state, as shown in Fig. 10(b). The response of Fe-SMA was comparable to that of CFRP. The average maximum force of Fe-SMA was 61.7 kN at a drift ratio of 2.71%, and it had about 2.5% higher strength than Control. As indicated by the envelope curves in Fig. 10(d), the post-peak response of the Fe-SMA was very close to that of CFRP. The retrofitted columns demonstrated that they still had fairly large load-carrying capacity beyond the ultimate point; however, the testing

was terminated at a 7% drift ratio. To estimate the cyclic deformation capabilities of the specimens, the displacement ductility factor (μ_d) proposed by Elnashai and Di Sarno (2008) was computed by using Eq. (7):

$$\mu_d = \frac{|\Delta_u^+| + |\Delta_u^-|}{|\Delta_y^+| + |\Delta_y^-|}, \tag{7}$$

where Δ_u^+ and Δ_u^- are the positive and negative displacements at ultimate state, respectively; Δ_y^+ and Δ_y^- are the positive and negative displacements at the yield point, respectively. μ_d of control, CFRP, and Fe-SMA columns were 1.99, 3.45, and 3.32, respectively. The test results clearly indicated that both retrofitting methods enhanced the deformation capacity of the seismically vulnerable RC column. In terms of μ_d, the Fe-SMA exhibited a considerable retrofitting effect. Furthermore, note that the Fe-SMA exhibited satisfactory performance, although its confinement pressure was half that of CFRP confinement.

To determine the variation in the damage level with the displacement increment, the secant stiffness was calculated at the first cycle of each drift ratio, as shown in Fig. 11. Fe-SMA initially had a slightly higher secant stiffness, followed by CFRP and Control. As the drift ratio increased, the secant stiffness of all specimens decreased at a relatively constant rate. At a drift ratio of 3%, Control had a secant stiffness of 1.15 kN/m at its ultimate point. The retrofitted columns continued to have similar responses, and the secant stiffnesses decreased as low as 0.39–0.41 kN/m at a 7% drift ratio. With respect to the global structural response, both CFRP and Fe-SMA could be considered to have sustained a comparable level of seismic damage.

3.3.2 Degradation of Columns Defined by UPV

Internal damage was defined as the compressional velocity of the ultrasound through the thickness of the columns. Fig. 12 presents the through-thickness velocities of each specimen averaged from all measurements during the loading cycles. To identify the velocity reduction, we normalized the velocities based on the initial measurements of each specimen. A greater velocity reduction was observed in the forced direction than in the non-forced direction. This was because more tensile stress was directly applied to the concrete at the side of the forced direction, causing cracking and faster degradation progress, and the direction of the damage influenced ultrasonic wave propagation. For Control, more than 80% of velocity reduction occurred at the sixth loading cycle because the ultrasonic waves barely propagated through the column. At the sixth loading cycle, both the CFRP and Fe-SMA specimens exhibited meaningful velocity reduction compared with the previous loading cycles owing to concrete damage. However, the retrofitting of the column prevented further damage in the concrete, resulting in only about 20% velocity reduction from both specimens. After the eighth loading cycle, the CFRP specimen exhibited a significant decrease and finalized

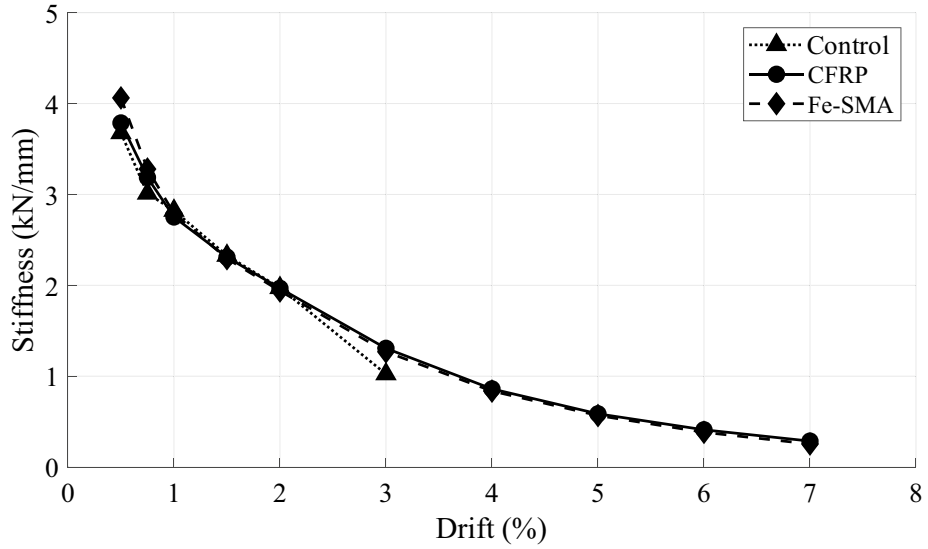

Fig. 11 Comparison of secant stiffness at each target drift ratio

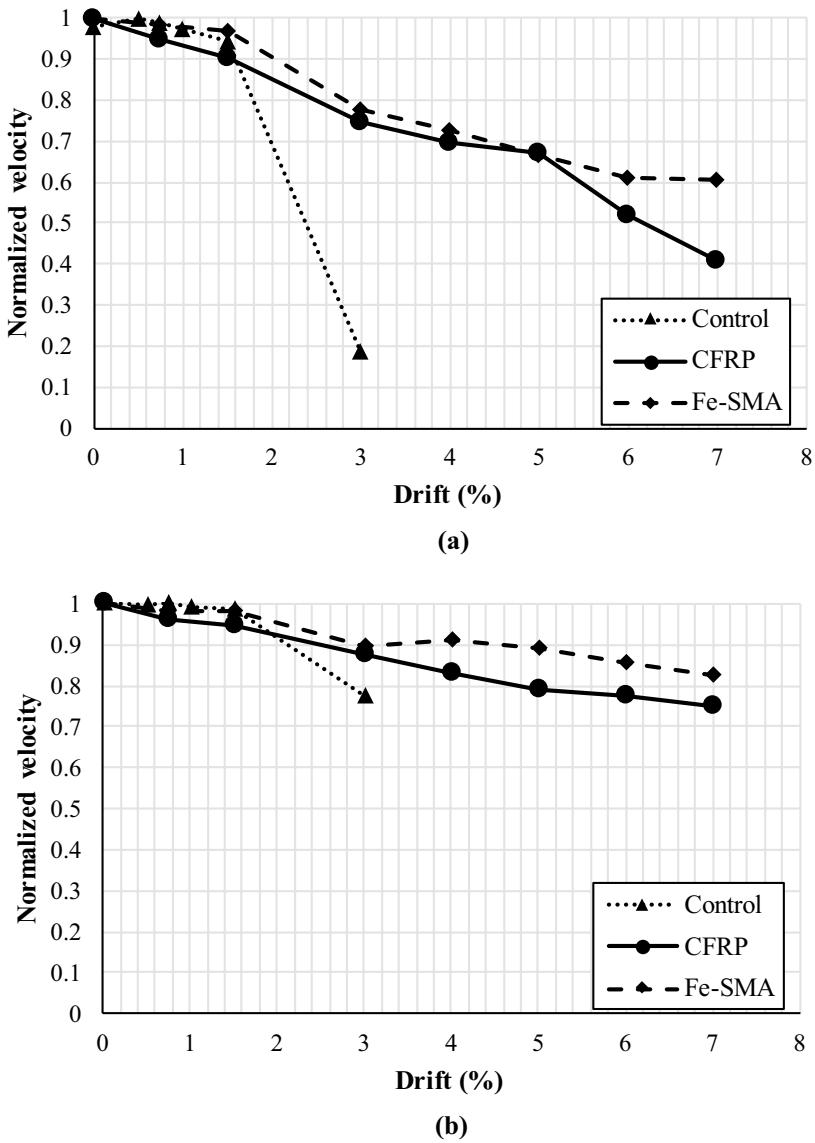

Fig. 12 Averaged through-thickness velocity: **a** forced direction; **b** non-forced direction

at a 60% velocity reduction, whereas Fe-SMA presented gradual degradation progress with only a 40% velocity reduction at the final stage. For the non-forced direction, less than 20% velocity reduction occurred at the final loading cycle for Fe-SMA, which implied minimal internal damage to concrete.

4 Discussion

4.1 Observation of Seismic Damages

Fig. 13 shows the damage status of the tested columns after the test. Visual inspection of seismic damages provides practical, valuable information for the decision-making process on damage estimation and post-earthquake restoration. In Fe-SMA, in which the concrete surface was partially visible, after horizontal tensile cracks developed in the plastic hinge region, the concrete damage did not progress further. However, Control experienced spalling of the cover concrete first in the plastic hinge region and eventually experienced shear failure with large diagonal concrete cracking. As shown in Fig. 13, the damage pattern of Fe-SMA markedly contrasted with that of Control. The pre-stressed

Fig. 13 External damages of concrete columns: **a** Control; **b** Fe-SMA

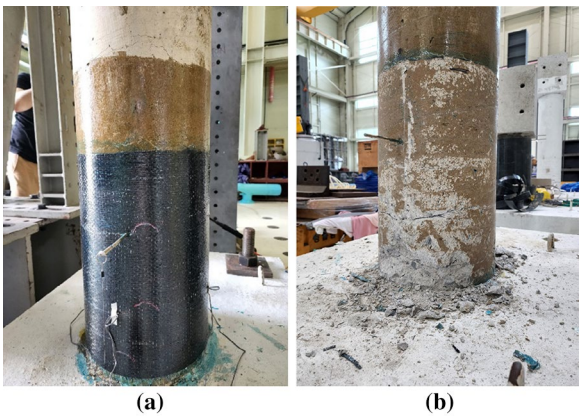

Fig. 14 CFRP specimen after failure: **a** with CFRP; **b** without CFRP

Fe-SMA strips, which actively confined the plastic hinge region, prevented the damage progress, resulting in the improved ductility of the column. However, for the specimen confined by the CFRP sheet, we could not conduct a visual inspection. Fig. 14 presents the damage status of CFRP with and without the CFRP sheets. Owing to the external CFRP sheets, although the column already reached its ultimate status, the damage could not be properly identified. After the CFRP sheets were removed, severely spalling concrete was observed at the bottom of the column.

The concrete damage at different locations was further evaluated based on the ultrasonic velocity measured at three locations above the column base. Owing to the plastic hinge during cyclic loading, the lower location of the column was expected to be more damaged.

Fig. 15 directly compares the progressive damage defined by the velocity reduction at different locations per specimen. For the control as shown in Fig. 15(a), all measurements significantly decreased by more than 80% after the maximum force of the column because the concrete was completely degraded. The retrofitted columns exhibited gradual degradation reduction rates after the maximum force of the columns. For Fe-SMA as described in Fig. 15(c), the velocity reductions at 5 and 15 cm consistently decreased with a constant slope of the line. Interestingly, the velocity reduction at 20 cm in Fe-SMA was significantly delayed and finalized with only a 30% decrease. This implied that the range of plastic hinges in the column was efficiently shortened under cyclic loading. The CFRP specimen exhibited different velocity reduction behaviors as shown in Fig. 15(b). From the locations at 5 and 15 cm in the CFRP specimen, the rate of velocity reduction was steeply modified after a 5% drift ratio, becoming higher than the reduction at 5 cm. This result indicated that the range of concrete damage widened with increasing seismic loading.

4.2 Global Structural Behavior of Columns Across Loading Cycles

The global structural behavior of all specimens was investigated using the secant stiffness of the column and the averaged through-thickness velocity, as shown in Fig. 16. With increasing loading levels, the stiffness of the columns generally decreased because of induced internal damage. The slopes of the lines indicate the degradation rates between measurements. The initial stiffness was similar among the columns, with that of the Fe-SMA being slightly higher than those of the others. The retrofitted columns exhibited notably different behaviors from the control, presenting significantly less load-induced degradation after a certain stiffness of 2.3 kN/mm. The controlled column significantly degraded with a slope of 0.579. For Fe-SMA, a minimal velocity reduction was observed, where the degradation rate was generally constant at 0.189. This behavior differed from that of CFRP, with two different degradation rates of 0.134 and 0.87. This was because the passive confinement effect was significantly reduced at higher loading levels. Consequently,

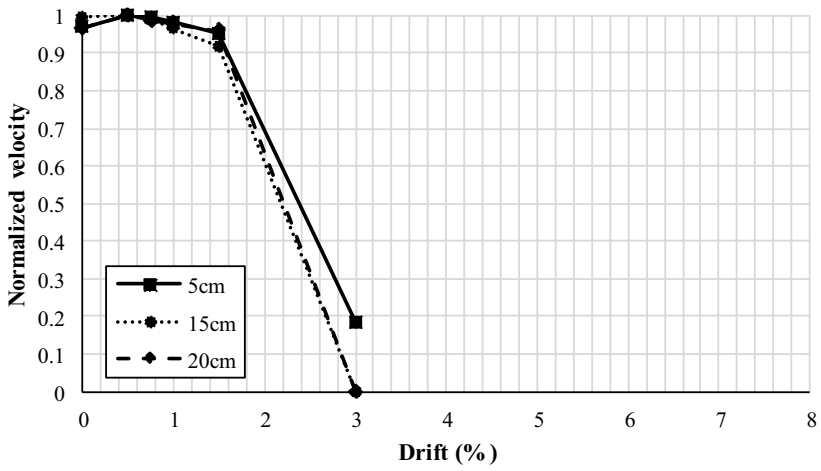

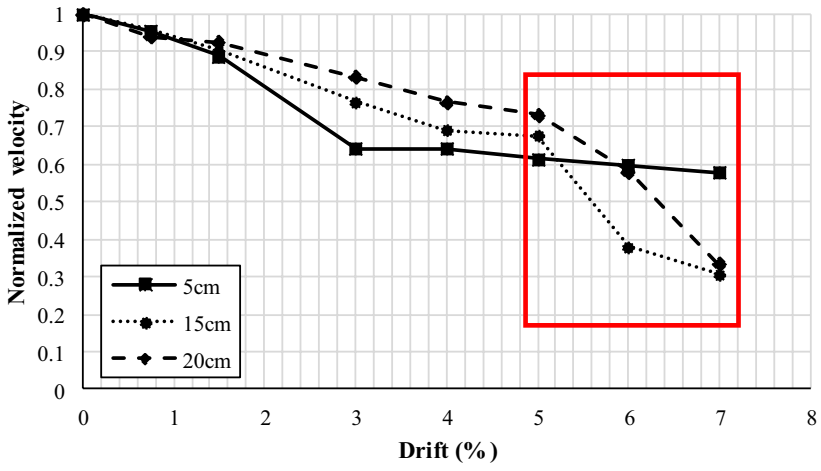

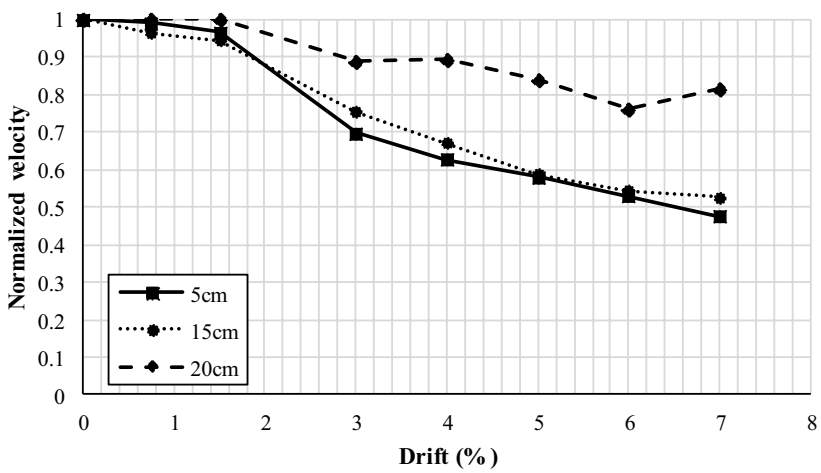

Fig. 15 Through-thickness velocity for **a** Control; **b** CFRP; **c** Fe-SMA

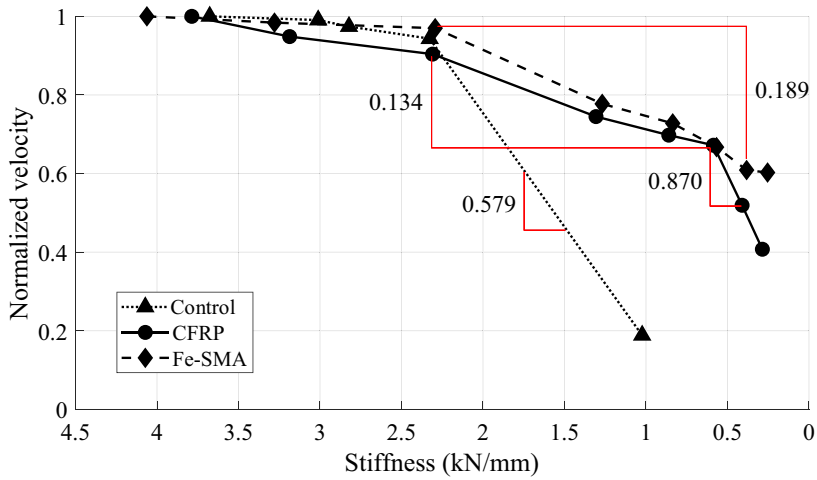

Fig. 16 Relationship between normalized through-thickness wave velocity and secant stiffness

the velocity reduction in Fe-SMA was finalized at only 40%. This was because the active confinement efficiently increased the ductility of the column under cyclic loading; thus, material degradation delayed.

5 Conclusions

In this study, the effect of SMA retrofitting on concrete columns was evaluated using the UPV test. Three concrete columns (the control, retrofitted by CFRP, and Fe-SMA) were investigated, and the through-thickness velocity was measured during cyclic loading. The findings reported in this paper demonstrate the ability of UPV test in obtaining meaningful degradation information for concrete. The data produced from the measurements enabled the quantification of the damage levels and evaluation of the retrofitting effect with respect to the degradation rate. Based on the results presented in this paper, the following conclusions were drawn:

1. Dry-coupled transducers for the UPV test enable to efficiently measure ultrasonic waves through a concrete column without additional coupling materials or procedures. The obtained through-thickness velocity is promising for the effective quantification of damage to RC columns after seismic events.
2. The column retrofitted with Fe-SMA exhibited distinct behavior to cyclic loading with respect to both the ductility and internal damage measured using the ultrasonic velocity compared with the control. The Fe-SMA specimen had a relatively lower velocity reduction and degradation rate during the entire loading cycle than the CFRP specimen.
3. From a practical perspective, unlike CFRP, Fe-SMAs have the benefits of an efficient retrofitting procedure and observable surface damage after seismic loading.

Appendix

See Tables 4 and 5.

Table 4 UPV data in the forced direction

Specimen no.		Control—forced direction			CFRP—forced direction			Fe-SMA—forced direction		
		5 cm	15 cm	20 cm	5 cm	15 cm	20 cm	5 cm	15 cm	20 cm
Before loading	1	4120	4105	4127	4340	4226	4192	4312	4294	4189
	2	4285	4188	4074	4371	4250	4180	4295	4046	4059
	3	4230	4089	4102	4329	4206	4193	4340	4027	4076
	Avg	4238	4104	4101	4347	4228	4188	4315	4122	4108
Cycle 1	1	4385	7107	4233	–	–	–	–	–	–
	2	4347	4157	4247	–	–	–	–	–	–
	3	4396	4095	4239	–	–	–	–	–	–
	Avg	4376	4120	4245	–	–	–	–	–	–
Cycle 2	1	4365	4096	4190	4010	4068	3970	4289	3976	4041
	2	4357	4054	4194	4348	4027	3973	4244	4010	4150
	3	4344	4102	4149	4060	4010	3851	4275	3919	4132
	Avg	4355	4084	4177	4139	4035	3931	4269	3968	4107
Cycle 3	1	4273	3977	4161	–	–	–	–	–	–
	2	4290	3980	4125	–	–	–	–	–	–
	3	4299	3950	4163	–	–	–	–	–	–
	Avg	4287	3969	4149	–	–	–	–	–	–
Cycle 4	1	4239	3768	4064	3750	3811	3885	4112	3909	4124
	2	4136	3820	4085	3788	3803	3872	4210	3847	4108
	3	4132	3743	4049	4034	3822	3852	4186	3900	4108
	Avg	4169	3777	4066	3854	3812	3869	4169	3885	4113
Cycle 6	1	800	–	–	2810	3273	3491	2922	3108	3627
	2	800	–	–	2783	3231	3483	3010	3103	3639
	3	–	–	–	2773	3206	3479	3075	3113	3670
	Avg	800	–	–	2788	3236	3484	3002	3108	3645
Cycle 7	1	–	–	–	2757	2980	3217	2652	2776	3803
	2	–	–	–	2790	2882	3194	3001	2759	3669
	3	–	–	–	2804	2893	3202	2455	2757	3521
	Avg	–	–	–	2783	2918	3204	2702	2764	3664
Cycle 8	1	–	–	–	2660	2892	3039	2410	2466	3392
	2	–	–	–	2663	2774	3057	2524	2406	3465
	3	–	–	–	2680	2879	3088	2574	2390	3485
	Avg	–	–	–	2667	2848	3061	2502	2420	3447

Table 4 (continued)

Specimen no.		Control—forced direction			CFRP—forced direction			Fe-SMA—forced direction		
		5 cm	15 cm	20 cm	5 cm	15 cm	20 cm	5 cm	15 cm	20 cm
Cycle 9	1	–	–	–	2578	2055	2940	2264	2193	2625
	2	–	–	–	2601	1433	1433	2035	2283	3344
	3	–	–	–	2596	1325	2923	2539	2237	3399
	Avg	–	–	–	2591	1604	2432	2279	2237	3122
Cycle 10	1	–	–	–	2520	1320	1540	2015	2116	3491
	2	–	–	–	2518	1267	1322	2107	2292	3267
	3	–	–	–	2503	1290	1320	2008	2096	3295
	Avg	–	–	–	2513	1292	1394	2043	2168	3351

Table 5 UPV data: non-forced direction

Specimen no.		Control—non forced direction			CFRP—non forced direction			Fe-SMA—non forced direction		
		5 cm	15 cm	20 cm	5 cm	15 cm	20 cm	5 cm	15 cm	20 cm
Before loading	1	4199	4163	4190	4337	4441	4178	4343	4087	4108
	2	4288	4155	4118	4383	4205	4237	4305	4116	4043
	3	4246	4097	4173	4344	4231	4234	4330	4181	4097
	Avg	4244	4138	4160	4355	4292	4217	4326	4128	4082
Cycle 1	1	4234	4151	4064	–	–	–	–	–	–
	2	4275	4120	4160	–	–	–	–	–	–
	3	4259	4107	4098	–	–	–	–	–	–
	Avg	4256	4126	4107	–	–	–	–	–	–
Cycle 2	1	4277	4071	4127	4199	4053	4114	4167	4027	4074
	2	4307	4127	4159	4235	4096	4068	4191	4089	4025
	3	4285	4151	4138	4226	4052	4092	4189	4004	4063
	Avg	4289	4116	4141	4220	4067	4091	4182	4040	4054
Cycle 3	1	4233	4036	4111	–	–	–	–	–	–
	2	4244	4121	4123	–	–	–	–	–	–
	3	4203	4135	4055	–	–	–	–	–	–
	Avg	4226	4097	4096	–	–	–	–	–	–
Cycle 4	1	4274	4106	4061	4164	3982	4023	4164	4019	4055
	2	4267	4087	4022	4229	3898	4024	4152	4038	4087
	3	4182	4074	4019	4106	3975	4041	4151	4055	4271
	Avg	4241	4089	4034	4166	3951	4029	4155	4037	4137
Cycle 6	1	3612	2651	3304	3612	3726	3939	3675	3730	3978
	2	3645	2651	3329	3618	3796	3886	3656	3332	4022
	3	–	2959	–	3594	3726	3938	3755	3457	3991
	Avg	3628	2753	3316	3608	3749	3921	3695	3506	4003
Cycle 7	1	–	–	–	3499	3440	3781	4026	3654	3966
	2	–	–	–	3495	3475	3741	3699	3665	3980
	3	–	–	–	3494	3523	3689	3709	3644	3968
	Avg	–	–	–	3496	3479	3737	3811	3654	3971
Cycle 8	1	–	–	–	3276	3358	3522	3553	3515	3945
	2	–	–	–	3289	3367	3530	3543	3541	4083
	3	–	–	–	3315	3324	3534	3787	3533	3941
	Avg	–	–	–	3293	3349	3528	3627	3529	3989
Cycle 9	1	–	–	–	3262	3267	3451	3484	3467	3849
	2	–	–	–	6148	3382	3443	3495	3417	3836
	3	–	–	–	3333	3231	3464	3439	3350	3857
	Avg	–	–	–	3247	3293	3452	3472	3411	3847
Cycle 10	1	–	–	–	3055	3224	3350	3159	3409	3776
	2	–	–	–	3051	3281	3385	3208	3393	3765
	3	–	–	–	3077	3151	3406	3234	3395	3762
	Avg	–	–	–	3061	3218	3380	3200	3399	3767

Acknowledgements
This research was supported by the Basic Science Research Program through the National Research Foundation of Korea (NRF) funded by a grant from the Korean government (MSIT) (No. 2021R1 A4A3030117) and the Korea Agency for Infrastructure Technology Advancement (KAIA) grant funded by the Ministry of Land, Infrastructure, and Transport (Grant 21CTAP-C164348-01).

Author contributions
TL: methodology, data curation, writing—original draft. SJ: data curation, investigation. UW: data curation, investigation. DJ: conceptualization, writing—original draft, review and editing, funding acquisition. HC: conceptualization, writing—original draft, review and editing, funding acquisition. All authors read and approved the final manuscript.

Author's information
Taemin Lee is a Ph.D. course student in the department of architecture of Soongsil University. He received B.S. degrees in the school of architecture from Soongsil University. His research interest focus on non-destructive testing in structural engineering. Saebyeok Jeong is a M.S. course student in the department of architectural engineering of Pusan University. She received B.S. degrees in the department of architectural engineering from Pusan University. Her research interest is the retrofitting reinforced concrete structure using smart materials. Ukyong Woo is a Ph.D. course student in the department of architecture of Soongsil University. He received B.S. degrees in the school of architecture from Soongsil University. His research interest focus on non-destructive testing in structural engineering. Hajin Choi is an assistant professor in the school of architecture of Soongsil University. He received a B.S., M.S. in architectural engineering from Soongsil University and a Ph.D. in civil engineering from University of Illinois Urbana-Champaign. His research interest is non-destructive testing methodology. Donghyuk Jung is an assistant professor in the school of civil, environmental and architectural Engineering of Korea University. He received B.S. degrees in the school of civil, environmental and architectural Engineering of Korea University, and M.S., Ph.D. in civil engineering from University of Illinois Urbana-Champaign. His research interest is the retrofitting reinforced concrete structure using smart materials.

Funding
National Research Foundation of Korea (NRF) grant funded by the Korea government (MSIT) (No. 2021R1 A4A3030117), and Korea Agency for Infrastructure Technology Advancement (KAIA) grant funded by the Ministry of Land, Infrastructure, and Transport (Grant 21CTAP-C164348-01).

Declarations

Competing interests
The authors declare no competing interests.

Author details
[1]School of Architecture, Soongsil University, Seoul, Republic of Korea. [2]Department of Architectural Engineering, Pusan National University, Busan, Republic of Korea. [3]School of Civil, Environmental and Architectural Engineering, Korea University, Seoul, Republic of Korea.

Received: 5 October 2022 Accepted: 16 November 2022
Published online: 24 February 2023

References

Akguzel, U., & Pampanin, S. (2012). Assessment and design procedure for the seismic retrofit of reinforced concrete beam-column joints using FRP composite materials. *Journal of Composites for Construction, 16*(1), 21–34.
American Concrete Institute. (2014). *Acceptance Criteria for Moment Frames Based on Structural Testing and Commentary (ACI 374.1-05, Reapproved 2014)* (pp. 1–9). Farmington Hills, MI: American Concrete Institute.
American Concrete Institute. (2017). *Guide for the design construction of externally bonded frp systems for strengthening concrete structures (ACI 440.2R-2017)*. Farmington Hills, MI, USA: ACI.
Architectural Institute of Korea (2018), A study on the earthquake disaster prevention for earthquake vulnerable buildings including piloti-type buildings, AIK-R-2018–848, pp. 7–8
ASTM. (2016), Standard test method for pulse velocity through concrete, ASTM C597–02. West Conshohocken, PA, USA.
California Department of Transportation. (2013). *Seismic design criteria version 1.7*. California Sacramento, CA: California Department of Transportation.
Chekroun, M., Le Marrec, L., Abraham, O., Durand, O., & Villain, G. (2009). Analysis of coherent surface wave dispersion and attenuation for non-destructive testing of concrete. *Ultrasonics, 49*(8), 743–751.
Choi, E., Chung, Y. S., Choi, D. H., & DesRoches, R. (2012). Seismic protection of lap-spliced RC columns using SMA wire jackets. *Magazine of Concrete Research, 64*(3), 239–252.
Cladera, A., Weber, B., Leinenbach, C., Czaderski, C., Shahverdi, M., & Motavalli, M. (2014). Iron-based shape memory alloys for civil engineering structures: An overview. *Construction and Building Materials, 63*, 281–293.
Czaderski, C., Shahverdi, M., Brönnimann, R., Leinenbach, C., & Motavalli, M. (2014). Feasibility of iron-based shape memory alloy strips for prestressed strengthening of concrete structures. *Construction and Building Materials, 56*, 94–105.
Di Sarno, L., Elnashai, A. S., & Nethercot, D. A. (2006). Seismic retrofitting of framed structures with stainless steel. *Journal of Constructional Steel Research, 62*(1–2), 93–104.
Elnashai, A. S., & Di Sarno, L. (2008). *Fundamentals of earthquake engineering*
Hong, K., Lee, S., Han, S., & Yeon, Y. (2018a). Evaluation of Fe-based shape memory alloy (Fe-SMA) as strengthening material for reinforced concrete structures. *Applied Sciences, 8*(5), 730. https://doi.org/10.3390/app8050730
Hong, K., Lee, S., Yeon, Y., & Jung, K. (2018b). Flexural response of reinforced concrete beams strengthened with near-surface-mounted Fe-based shape-memory alloy strips. *International Journal of Concrete Structures and Materials, 12*(1), 1–13. https://doi.org/10.1186/s40069-018-0279-y
Hong, K., Yeon, Y., Shim, W., & Kim, D. (2020). Recovery behavior of fe-based shape memory alloys under different restraints. *Applied Sciences*, *10*(10), 3441.
Janke, L., Czaderski, C., Motavalli, M., & Ruth, J. (2005). Applications of shape memory alloys in civil engineering structures—Overview, limits and new ideas. *Materials and Structures, 38*(5), 578–592.
Ji, S. W., Yeon, Y. M., & Hong, K. N. (2020). Compression behavior of concrete laterally confined by Fe-based shape memory alloy spiral reinforcement. *Journal of the Korean Society for Advanced Composites Structures., 11*(6), 63–70. https://doi.org/10.11004/kosacs.2020.11.6.063
Jung, D., Wilcoski, J., & Andrawes, B. (2018). Bidirectional shake table testing of RC columns retrofitted and repaired with shape memory alloy spirals. *Engineering Structures, 160*, 171–185.
Kim, S., Moon, T., & Kim, S. J. (2020). Effect of uncertainties in material and structural detailing on the seismic vulnerability of RC frames considering construction quality defects. *Applied Sciences, 10*(24), 8832.
Ma, C. K., Apandi, N. M., Sofrie, C. S. Y., Ng, J. H., Lo, W. H., Awang, A. Z., & Omar, W. (2017). Repair and rehabilitation of concrete structures using confinement: A review. *Construction and Building Materials, 133*, 502–515.
Naik, T., Malhotra, V., & Popovics, J. (2004). *The ultrasonic pulse velocity method. In Handbook on nondestructive testing of concrete*. CRC Press.
Ohdaira, E., & Masuzawa, N. (2000). Water content and its effect on ultrasound propagation in concrete—the possibility of NDE. *Ultrasonics, 38*(1–8), 546–552.
Rojob, H., & El-Hacha, R. (2017). Self-prestressing using iron-based shape memory alloy for flexural strengthening of reinforced concrete beams. *ACI Structural Journal, 114*(2), 523.
Saadatmanesh, H., Ehsani, M. R., & Li, M. W. (1994). Strength and ductility of concrete columns externally reinforced with fiber composite straps. *Structural Journal, 91*(4), 434–447.
Saffar, S., & Abdullah, A. (2013). Longitudinal wave propagation in multi cylindrical viscoelastic matching layers of airborne ultrasonic transducer: New method to consider the matching layer's diameter (frequency< 100 kHz). *Ultrasonics, 53*(6), 1174–1184.
Seible, F., Priestley, M. N., Hegemier, G. A., & Innamorato, D. (1997). Seismic retrofit of RC columns with continuous carbon fiber jackets. *Journal of Composites for Construction, 1*(2), 52–62.
Shahverdi, M., Czaderski, C., & Motavalli, M. (2016). Iron-based shape memory alloys for prestressed near-surface mounted strengthening of reinforced concrete beams. *Construction and Building Materials, 112*, 28–38.
Shehata, I. A., Carneiro, L. A., & Shehata, L. C. (2002). Strength of short concrete columns confined with CFRP sheets. *Materials and Structures, 35*(1), 50–58.
Shin, M., & Andrawes, B. (2010). Experimental investigation of actively confined concrete using shape memory alloys. *Engineering Structures, 32*(3), 656–664.
Shin, M., & Andrawes, B. (2011). Lateral cyclic behavior of reinforced concrete columns retrofitted with shape memory spirals and FRP wraps. *Journal of Structural Engineering, 137*(11), 1282–1290.
Suhail, R., Amato, G., & McCrum, D. P. (2020). Active and passive confinement of shape modified low strength concrete columns using SMA and FRP systems. *Composite Structures, 251*, 112649.
Vahidpour, M., Kheyroddin, A., & Kioumarsi, M. (2022). Experimental Investigation on Flexural Capacity of Reinforced Concrete Beams Strengthened with 3D-Fiberglass, CFRP and GFRP. *International Journal of Concrete Structures and Materials, 16*(1), 1–20.

Xiao, Y., & Wu, H. (2003). Retrofit of reinforced concrete columns using partially stiffened steel jackets. *Journal of Structural Engineering, 129*(6), 725–732.
Yahiaoui, D., Saadi, M., & Bouzid, T. (2022). Compressive Behavior of Concrete Containing Glass Fibers and Confined with Glass FRP Composites. *International Journal of Concrete Structures and Materials, 16*(1), 1–19.
Zerbe L, Reda M, Dawood M, Belarbi A, Senouci A, Gencturk B, Michel J. (2017). *Behavior of retrofitted concrete members using iron-based shape memory alloys* [Conference presentation]. Fourth Conference on Smart Monitoring, Assessment and Rehabilitation of Civil Structures.
Zhao, J., Shen, F., Si, C., Sun, Y., & Yin, L. (2020). Experimental investigation on seismic resistance of RC shear walls with CFRP bars in boundary elements. *International Journal of Concrete Structures and Materials, 14*(1), 1–20.

Publisher's Note